crystals

MDPI

Article

One-Pot Synthesis of Zinc-Doped Mesoporous Silica

Hajar Jabkhiro [1,2], Mario Luigi Naitana [1], Eleonora Marconi [2,3], Federica Bertelà [1], Giovanna Iucci [1], Ilaria Carlomagno [4], Chiara Battocchio [1], Carlo Meneghini [1,*] and Luca Tortora [1,2]

1 Department of Science, Roma Tre University, via della Vasca Navale 84, 00146 Rome, Italy; hajar.jabkhiro@uniroma3.it (H.J.); marioluigi.naitana@uniroma3.it (M.L.N.); federica.bertela@uniroma3.it (F.B.); giovanna.iucci@uniroma3.it (G.I.); chiara.battocchio@uniroma3.it (C.B.); luca.tortora@uniroma3.it (L.T.)
2 INFN Roma Tre, via della Vasca Navale 84, 00146 Rome, Italy; eleonora.marconi@roma3.infn.it
3 Centro di Eccellenza—DTC Lazio, Piazzale Aldo Moro, 5, 00185 Rome, Italy
4 Elettra Sincrotrone Trieste, SS 14 km 163.5, 34149 Trieste, Italy; ilaria.carlomagno@elettra.eu
* Correspondence: carlo.meneghini@uniroma3.it

Abstract: This paper presents an original method for synthesizing Zn-doped mesoporous silica (KCC-1) via a one-pot microemulsion method followed by hydrothermal treatment. Zn incorporation into the silica matrix was achieved by varying Zn/Si molar ratios from 1% to 8%. The Zn-doping effect on KCC-1 morphological and structural properties was investigated using several characterization techniques, providing new insights into the Zn-doping behavior and coordination environment. X-ray fluorescence (XRF) spectra confirmed the stoichiometric doping of silica nanoparticles for samples obtained with a precursor concentration of 1%, 3%, and 6%. An attenuated total reflectance Fourier transform infrared (ATR-FTIR) spectroscopy highlighted that Zn was included into the KCC-1 matrix rather than chemically adsorbed onto the surface. Scanning electron microscopy (SEM) images clearly showed that a low Zn content preserves the KCC-1 fibrous morphology. An X-ray diffraction (XRD) analysis confirmed the amorphous nature of the doped nanoparticles, suggesting a structural disorder of the silica framework at higher Zn concentrations. X-ray photoelectron spectroscopy (XPS) revealed that Zn–$(OH)_2$ bonds increased at a 6% Zn/Si molar ratio, confirming the disordered inclusion of Zn at this doping limit. X-ray absorption near-edge structure (XANES) data revealed that in Zn-doped silica at 3% and 6%, Zn primarily exists in a coordination state similar to zinc-silicates and the amorphous Zn-hydroxyapatite-like phase.

Keywords: mesoporous silica nanoparticles; zinc incorporation; hydrothermal synthesis; amorphous nanostructures; XANES

Academic Editor: Vladimir Chigrinov

Received: 26 December 2024
Revised: 14 January 2025
Accepted: 16 January 2025
Published: 21 January 2025

Citation: Jabkhiro, H.; Naitana, M.L.; Marconi, E.; Bertelà, F.; Iucci, G.; Carlomagno, I.; Battocchio, C.; Meneghini, C.; Tortora, L. One-Pot Synthesis of Zinc-Doped Mesoporous Silica. *Crystals* **2025**, *15*, 100. https://doi.org/10.3390/cryst15020100

1. Introduction

Since the introduction of Stöber silica [1], various synthesis methods have emerged to create mesoporous silica materials with well-defined hexagonal pores [2], tunable and larger pores [3], and composite structures [4]. In 2010, the discovery of dendritic fibrous nano-silica, referred to as KAUST Catalysis Center-1 (KCC-1) [5], introduced colloidal spheres formed by a unique radial 3D arrangement of dendritic fibers [6]. This morphology reduces pore blocking and provides a substantial surface area, enabling an easier access to active sites [7]. Moreover, the special thermal and hydrothermal stability, and mechanical resilience of KCC-1 nanoparticles, make them suitable for a wide range of applications including heterogenous catalysis, solar energy harvesting, energy storage, CO_2 valorization, and drug delivery [8].

The incorporation of inorganic ions such as transition metals [9], rare earth elements [10], and various metal oxides [11–13], has been extensively explored to enhance the functionality and fine-tune the properties of KCC-1-based nanomaterials for specific applications, particularly in heterogenous catalytic processes. For instance, silver nanoparticles supported on KCC-1 have been used for the hydrogenation of dimethyl oxalate [14], while palladium-supported KCC-1 has proven effective in Suzuki cross-coupling reactions [15]. Additionally, iron-doped KCC-1 has shown promise in the catalytic ozonation of sulfamethazine [16], and bi-metallic systems, such as Ni-Co-loaded KCC-1, have been applied in methane dry reforming [17].

The incorporation of transition metal ions into the silica framework has been investigated over the last few decades due to their applications in eco-friendly and industrially important catalytic reactions [18]. Zinc (Zn), in particular has been considered as a promising candidate for doping mesoporous silica, owing to its application in diverse fields such as optoelectronics [19], sensing [20], biology [21], and catalysis [22]. Zn oxide nanostructures are also valued for their photo-conducting [23], electrical, and optical properties [24].

Metal-loaded silica nanomaterials are commonly prepared through post-synthesis modification, particularly by the wet impregnation method. Notably, KCC-1 impregnated with Zn oxide was reported for CO_2 methanation [25] and the hydroisomerization of n-hexane [9], among others. However, the impregnation method can lead to an uneven distribution of metal particles, reduced surface area, and pore blocking [26–28].

To address these challenges, a one-pot synthesis approach presents exciting possibilities for the efficient and sustainable synthesis of metal-doped KCC-1. This method integrates doping and material formation in a single step, ensuring uniform dopant distribution, reducing costs, and improving time efficiency. It also offers better control over morphology, enhances dopant-matrix interactions, minimizes waste, and optimizes the catalytic performance of the material.

To the best of our knowledge, the one-pot hydrothermal synthesis of Zn-doped KCC-1 has not yet been reported. This approach could offer synergistic effects by combining the open fibrous structure of KCC-1 with the generation of new active sites within the siliceous framework without limiting the pore accessibility, all through one simple and economical approach. In this work, we address this gap by utilizing zinc acetate as the zinc precursor to directly incorporate Zn ions into the silica matrix during synthesis. We systematically investigated the influence of varying Zn loading percentages on the morphological and structural properties of KCC-1, employing a range of advanced characterization techniques. This study represents a critical step toward optimizing the material for its potential applications.

2. Materials and Methods

2.1. Materials and Nanoparticles Synthesis

The following chemicals were purchased from Merck S.r.l. (Darmstadt, Germany) and used without further purification: tetraethyl orthosilicate (TEOS) as the silica source, cationic surfactant cetylpyridinium bromide (CPB) as the template, 1-pentanol as co-surfactant, urea as the hydrolyzing agent, cyclohexane as the oil phase, zinc acetate dihydrate as the zinc precursor, deionized water (DIW), isopropyl alcohol (IPA), and acetone.

Pure KCC-1 and Zn-doped KCC-1 nanomaterials were synthesized using a modified one-pot template-based microemulsion method followed by hydrothermal treatment [29]. Samples were prepared with Zn/Si molar ratios ranging from 1 to 8%. In a typical synthesis, 0.5 g (0.0013 mol) of CPB was dissolved in 15 mL of cyclohexane and 0.75 mL (0.0068 mol) of pentanol to form the oil phase. The mixture was stirred at room temperature for 30 min to ensure complete dissolution. Simultaneously, the aqueous phase was prepared by

dissolving the appropriate amount of Zn acetate along with 0.3 g (0.004 mol) of urea in 15 mL of DIW. This solution was then added to the oil phase under vigorous stirring, followed by the dropwise addition of 1.25 g (0.006 mol) of TEOS. After 30 min of stirring, the resulting emulsion was transferred to a Teflon-lined autoclave and thermally treated at 120 °C for 4 h. The product was recovered via centrifugation at 6000 rpm for 20 min, washed three times with DIW and IPA mixtures, once with acetone, and then air-dried at room temperature. A final calcination at 550 °C for 6 h with a 3 °C/min heating ramp removed the template. Pure KCC-1 was synthesized similarly but without the Zn source. The synthesized samples were denoted as X-ZnKCC-1 (X = Zn/Si molar ratio).

2.2. Chemical, Morphological, and Structural Characterization

An X-ray fluorescence (XRF) analysis (Olympus Vanta C Series) was employed to determine the elemental composition of the synthesized nanomaterials. A 50 kV X-ray tube with a silver (Ag) anode and silicon drift detector was used. The measurements were performed using two X-ray beams, operating at 9.9 kV and 40 kV with a data acquisition of 60 s per beam.

Attenuated total reflectance Fourier transform infrared (FTIR-ATR) spectroscopy analysis (ThermoFisher®Nicolet iS50 FTIR instrument, Thermo Fisher Scientific, Waltham, MA, USA) was used to identify the surface functional groups collecting spectra directly on milled powder samples with a 4 cm^{-1} resolution over the 400–4000 cm^{-1} range.

Field emission scanning electron microscopy FE-SEM (ZEISS SIGMA 300, Carl Zeiss AG, Oberkochen, Germany) provided detailed insights into the morphological features of the nanoparticles. Images were collected at an accelerating voltage of 10 kV. ImageJ software 1.54g was employed to analyze these images and provide the dimensional parameters of the particles.

Crystallographic phases were determined using a Rigaku Smartlab SE diffractometer (Rigaku Smart Lab, Rigaku Corporation, Tokyo, Japan) within the 2θ range of 10–80° at a 3 min^{-1} rate using Cu K_α radiation (λ = 1.54 Å).

X-ray photoelectron spectroscopy (XPS) was used to assess the surface chemistry using a laboratory instrument, consisting of Ultra High Vacuum (UHV) chambers separated by a gate valve. The analysis chamber was equipped with a hemispherical electron analyzer providing a resolution of 1 eV at the Ag $3d_{5/2}$ core level. Detector energy was achieved referencing spectra to the C 1s core level at 285.0 eV, for all samples. Samples were outgassed overnight at 10^{-8} Torr before analysis. A non-monochromatized Mg K_α (1253.6 eV) X-ray source was used, and atomic ratios were calculated using Scofield's cross-section values. A curve-fitting of the C 1s, O 1s, Si 2p, and Zn 2p spectra was performed using Gaussian profiles, with spin-orbit splitting values of 0.60 eV for Si 2p and 23.10 eV for Zn 2p, maintaining a consistent full width at half maximum (FWHM) for spin-orbit components and fixed branching ratios of 2 for Si $2p_{3/2}$/Si $2p_{1/2}$ and Zn $2p_{3/2}$/Zn $2p_{1/2}$.

The chemical selectivity and local atomic structure sensitivity of X-ray absorption fine spectroscopy (XAFS) [30] provide valuable details about the fate of Zn ions in the samples. This information is crucial for evaluating the nature of the Zn dopant in the mesoporous samples. Zn K edge X-ray absorption spectra were collected at the XRF beamline of the Elettra synchrotron radiation facility [31] in fluorescence standard geometry. A silicon drift detector (XFlash 5030, Bruker Nano GmbH, Berlin, Germany) was used in the vacuum chamber available at the beamline [32]. The primary beam intensity was measured using a system developed by the Elettra Detector group, based on a polycrystalline diamond plate system (plate by Dectris, Baden-Daettwil, Switzerland). Due to beamtime constraints, the data collection focused on the near-edge (XANES) regions. The raw absorption data were processed following standard background subtraction and edge discontinuity normal-

ization [33], and then quantitatively analyzed using the linear combination fitting (LCF) method [34]. This technique is particularly effective for XANES data analysis, enabling the quantification of complex mixtures and the detection of subtle variations in electronic or local structural environments [35]. XAS data treatment and fitting was performed using Athena software from the Demeter 0.9.26 package [36].

3. Results and Discussion

3.1. Synthesis of Pure KCC-1 and Zn-Doped KCC-1

The synthesis protocol reported above and here represented in Figure 1 successfully produced Zn-doped KCC-1 nanoparticles, as then evidenced by morphological and structural analyses. The use of CPB as a structure-directing agent, along with TEOS as a silica precursor, induced the formation of fibrous silica spheres characteristic of KCC-1. The incorporation of Zn, achieved through the precise control of Zn/Si molar ratios in the aqueous phase, resulted in homogeneous doping as confirmed by subsequent characterization techniques. Calcination at 550 °C ensured the removal of organic template, yielding porous structures. The Zn doping did not compromise the fibrous architecture of KCC-1 for the percentages of zinc acetate from 1% to 6%. The dendritic fibrous morphology was completely lost for a higher percentage of zinc precursor. Notably, increasing Zn/Si ratios produced consistent trends in structural and compositional attributes, highlighting the tunability of the method. The details of the obtained materials, including doping ratios and synthesis conditions, are summarized in Table 1. Figure 1 illustrates the key steps of the synthesis, emphasizing the role of hydrothermal treatment in achieving the desired nanostructures.

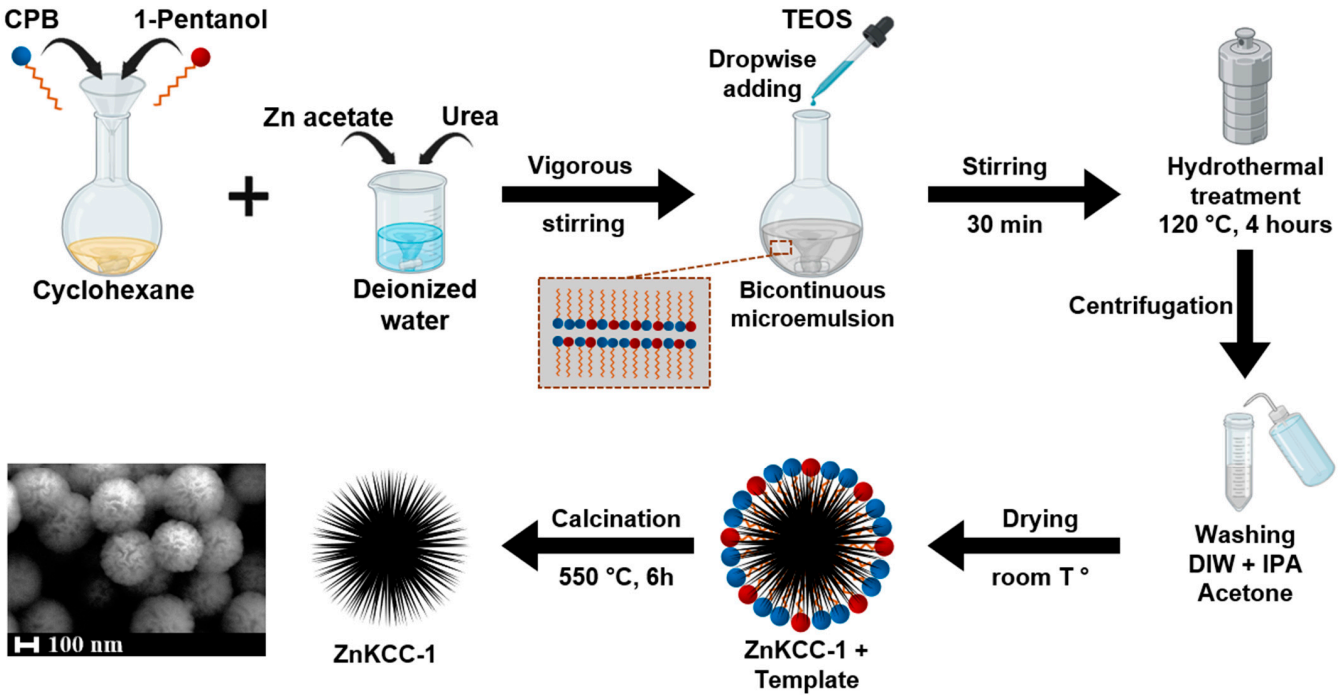

Figure 1. Schematic of Zn-doped KCC-1 synthesis via microemulsion followed by hydrothermal treatment.

Table 1. List of the synthesized samples.

Sample	Zn/Si (% mol) [1]	Reaction Temperature	Reaction Time	Calcination
KCC-1	0	120 °C	4 h	550 °C—6 h
1-ZnKCC-1	1			
3-ZnKCC-1	3			
6-ZnKCC-1	6			
8-ZnKCC-1	8			

[1] The other chemicals used were identical in all cases: DIW (15 mL), cyclohexane (15 mL), 1-pentanol (0.75 mL), CPB (0.5 g), urea (0.3 g), and TEOS (0.006mol).

3.2. X-Ray Fluorescence

To confirm the presence and successful incorporation of Zn in the synthesized nanoparticles, the elemental analysis was performed using XRF spectroscopy on KCC-1 samples, both pure and doped with zinc. The obtained spectra and the Zn/Si molar ratios are presented in Figure 2 and Table 2, respectively. The peaks observed at 2.97 and 3.15 keV are attributed to the L_α and L_β emission lines of Ag arising from the use of a silver anode as the X-ray source. The XRF spectra (Figure 2) revealed a characteristic peak detected at 1.74 (Si K_α) across all samples, consistent with the expected emission line of silicon [37]. Additionally, tiny traces of the template CPB used during the synthesis were detected at 11.92 keV related to Br K_α emission, suggesting that the template was not fully removed during the washing and calcination steps. As the zinc concentration increased, a corresponding increase in the intensity of Zn K_α (8.63 keV) and Zn K_β (9.57 keV) emission lines was observed.

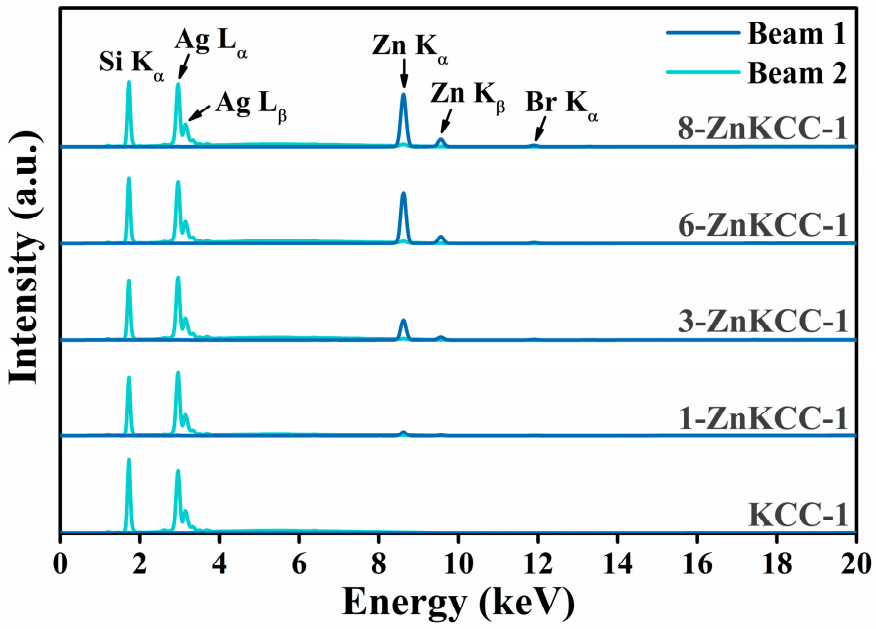

Figure 2. XRF spectra of the nanoparticles.

Table 2. The calculated Zn/Si molar ratios of the prepared Zn-doped KCC-1 samples.

Sample	1-ZnKCC-1	3-ZnKCC-1	6-ZnKCC-1	8-ZnKCC-1
Zn/Si (mol %)	0.7 ± 0.2	2.8 ± 0.5	6.2 ± 1.1	6.32 ± 1.2

The XRF analysis was performed four times for each sample; the average Zn/Si values along with the associated standard uncertainties are reported in Table 2. The experimental

Zn/Si molar ratio was consistent with the expected ratio for all samples except for 8-ZnKCC-1, where the molar fraction Zn/Si was lower than expected. This suggests that increasing the zinc precursor concentration did not result in a proportional increase in Zn loading within the silica matrix, possibly indicating a maximum Zn doping limit of 6% within the silica framework. Furthermore, the uncertainty of the experimental Zn/Si ratio doubled as this limit was approached in 6- and 8-ZnKCC-1 samples, indicating a less homogenous distribution of Zn within the silica matrix.

3.3. ATR-FTIR

The vibrational spectroscopy of the pure KCC-1 and Zn-doped KCC-1 was determined by ATR-FTIR. The spectra of the samples in the range 400–4000 cm^{-1} are depicted in Figure 3. The broad bands at 3400 and 1635 cm^{-1} observed in all samples are attributed to the O–H stretching and H–O–H bending vibrations. These peaks are indicative of the presence of a small amount of moisture (H_2O) content on the surface of the particles. All samples show the four characteristic bands of the silica framework: 1062 cm^{-1} and 800 cm^{-1} attributed to the asymmetric and symmetric Si–O–Si stretching vibrations, 970 cm^{-1} corresponding to the external silanol groups (Si–OH), and 450 cm^{-1} related to Si–O–Si bending vibrations [38]. To indicate the formation of a Si–O–Zn bond by the replacement of H atoms of the terminal –OH by the metal ions, the silanol band at 970 cm^{-1} should decrease [9,12,38], which was not the case in our samples indicating that Zn was not chemically adsorbed onto the surface of KCC-1, but physically included into the matrix.

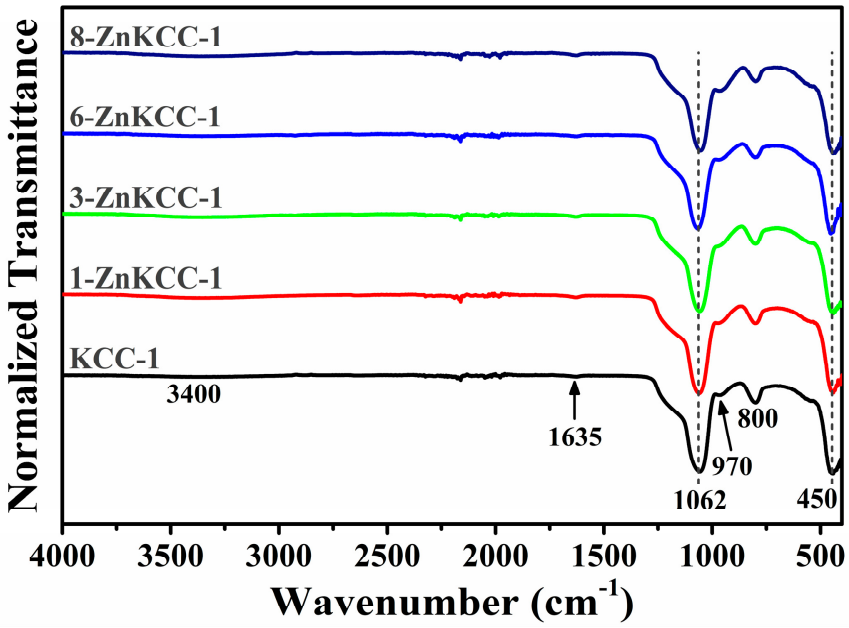

Figure 3. FTIR spectra of the nanoparticles.

3.4. Field Emission Scanning Electron Microscopy

SEM analysis was employed to evaluate the morphological features of the Zn-doped nanoparticles. The SEM image of KCC-1 (Figure 4(a_1)) display the characteristic fibrous and spherical morphology previously reported [29], with distinct fibers radiating outward from the center. The particle size distribution (Figure 4(a_2)) shows a narrow peak with an average particle size (APS) of ~399 nm, indicating a uniform size distribution. At 1% Zn doping (Figure 4(b_1)), the structure appears uniform with well-defined spherical particles and uniform fibrous networks. The size of the yielded nanoparticles is consistent, ranging around 200–400 nm, with a slight decrease of the APS to ~318 nm (Figure 4(b_2)), indicating a minimal disruption at this low Zn doping level. As the Zn content increased to 3% and

6% (Figure 4(c_1,d_1)), the overall spherical morphology and size distribution were retained, while the fiber density decreased. The APS further decreased (Figure 4(c_2,d_2)), with a broader distribution, reflecting an increased particle size variability as Zn doping increases. These changes suggest that a higher Zn incorporation may influence the integrity of the silica framework by altering the condensation process, likely due to Zn competing with silanol groups during the hydrolysis or interactions between Zn ions and the silica network. At the highest Zn-doping of 8% (Figure 4(e_1)), the particles exhibited a dense and aggregated morphology, the fibrous features were less prominent, and only a limited number of well-defined mesoporous nanoparticles was observed. The particle size uniformity was significantly reduced with the broadest (bimodal) distribution (Figure 4(e_2)). This trend suggests that the incorporation of higher levels of zinc influenced the integrity, growth, and aggregation behavior of the nanoparticles. Overall, SEM images (Figure 4) show that the silica nanoparticles exhibit consistent morphologies and a homogeneous contrast, even as the Zn content increases. Notably, no particles with distinct morphologies, which could indicate the presence of Zn-rich phases, were observed. This finding, coupled with the significant contrast difference between Zn and Si, which would make compositional changes evident, strongly argues against any Zn segregation within the silica matrix or the formation of separate Zn-rich nanoparticles.

3.5. X-Ray Diffraction

XRD analysis was performed on both pure KCC-1 and Zn-doped samples to investigate their structural properties (Figure 5). The XRD patterns of all of the samples revealed an overall amorphous structure, characterized by a broad halo in the 2θ range of 15–30°, attributed to the amorphous silica framework [38]. Notably, no sharp peaks indicative of crystalline phases were observed. This result confirms that Zn doping does not alter the amorphous nature of KCC-1 mesoporous silica [39], suggesting that Zn ions are evenly distributed into the silica matrix or physiosorbed on the surface of KCC-1. Moreover, the absence of distinct peaks corresponding to the Wurtzite ZnO structure indicates that the doping concentration is insufficient to induce phase separation. A closer examination of the diffractograms reveals a slight broadening of the amorphous diffraction halo and the emergence of additional weak oscillations close to the main diffraction peak with increasing Zn content. These observations suggest that high Zn doping subtly influences the structure of the silica matrix. This behavior aligns with the results of a study in which doping amorphous silica with Ni ions via a one-pot synthesis also resulted in the broadening of XRD peaks, attributed to the distortion of the fibrous silica framework [40].

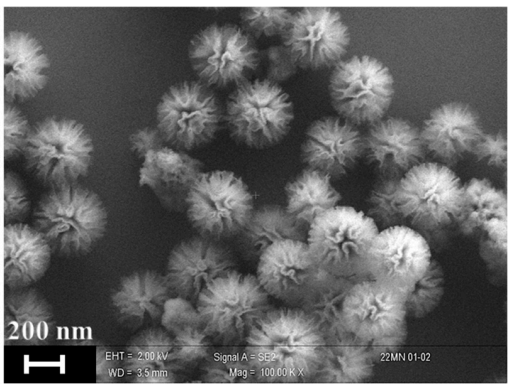

(**a**1)

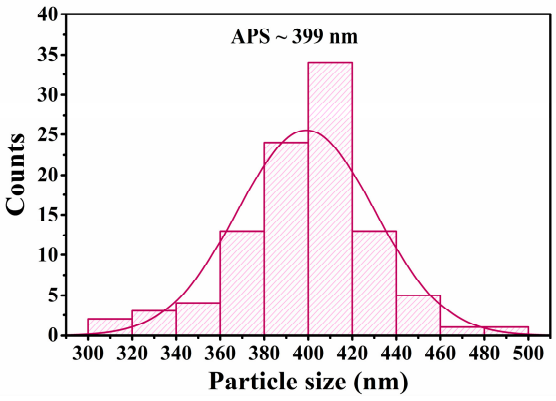

(**a**2)

Figure 4. *Cont.*

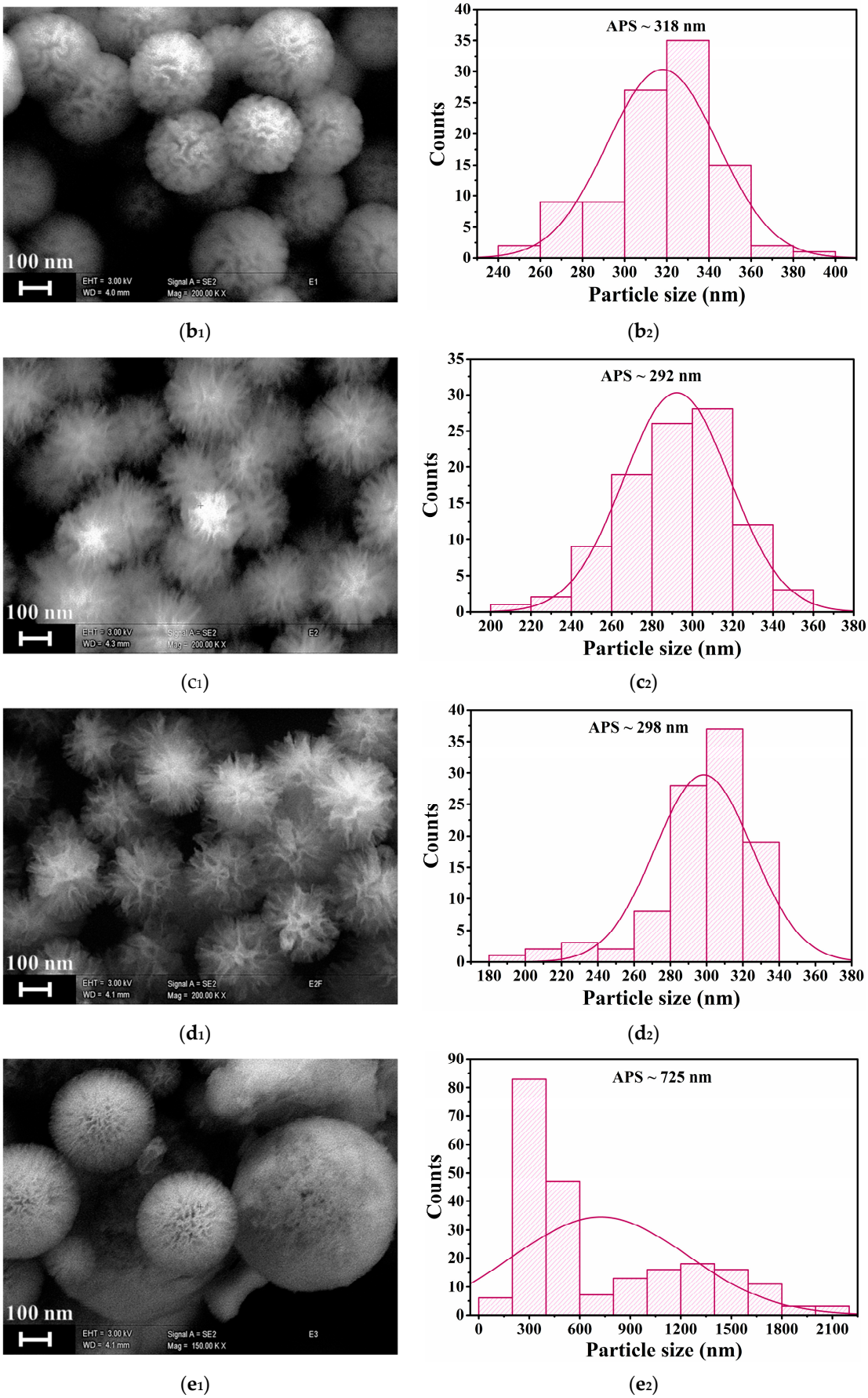

Figure 4. SEM images and particle size distribution of the following: (**a**) KCC-1; (**b**) 1-ZnKCC-1; (**c**) 3-ZnKCC-1; and (**d**) 6-ZnKCC-1; and (**e**) 8-ZnKCC-1.

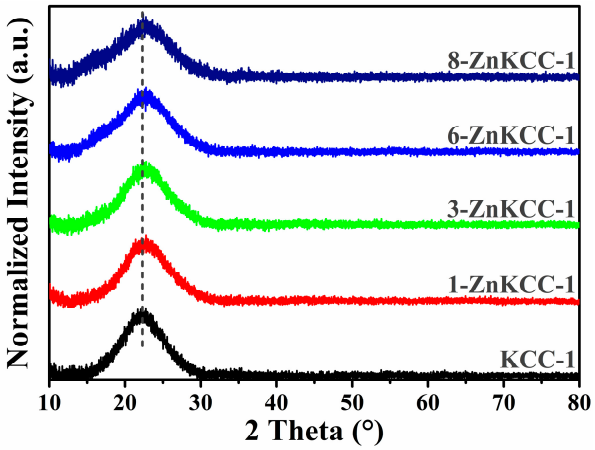

Figure 5. XRD patterns of pure (KCC-1) and Zn-doped (*x*-ZnKCC-1) nanoparticles.

3.6. X-Ray Photoelectron Spectroscopy

The coordination state of the surface elements of the 3-ZnKCC-1 and 6-ZnKCC-1 samples was investigated using XPS. The spectra were collected at the C 1s, O 1s, Zn 2p and Si 2p core levels, as shown in Figure 6.

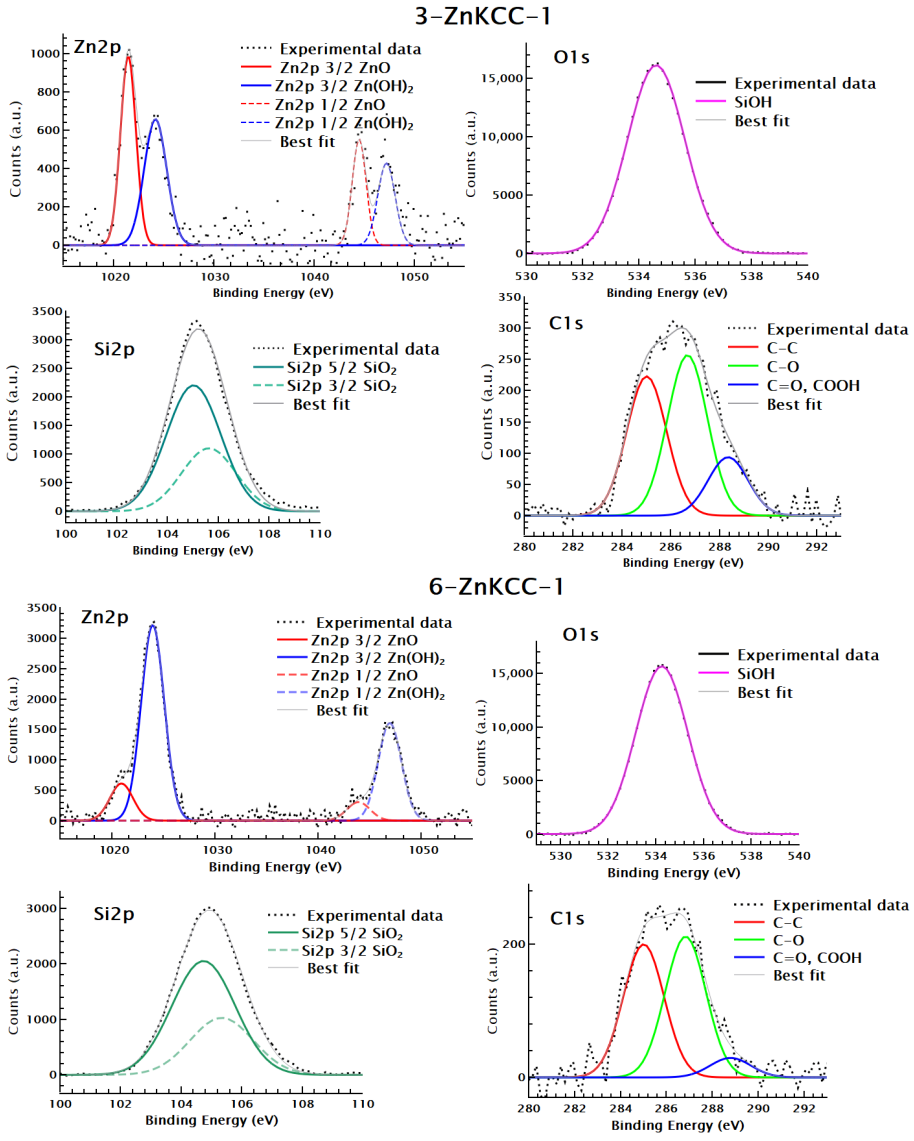

Figure 6. XPS profiles of Zn 2p, O 1s, Si 2p, and C 1s in 3Zn-KCC-1 and 6Zn-KCC-1.

The C 1s spectra of 3-ZnKCC-1 and 6-Zn-KCC-1 revealed three distinct components at binding energies of 285, 286.7, and 288 eV, corresponding to C–C, C–O and C=O, COOH bonds, respectively. The Si 2p profile exhibited a single peak centered at approximately 105 eV, indicative of Si–O bonds in SiO_2. This result confirms the successful formation and growth of the SiO_2 fibrous shell [41].

A deconvolution of the Zn 2p spectra revealed the presence of two types of zinc ions, either bonded to oxygen (Zn–O) or bonded to hydroxyl groups (Zn–$(OH)_2$) at 1021 and 1024 eV BE, respectively. Notably, an increase in the intensity ratio of Zn–$(OH)_2$ was observed as the Zn content increased to 6%. Consistent with the XRF result, at the 6% doping limit, the distribution of Zn becomes less homogenous, leading to a higher surface concentration of Zn compared to the 3% sample.

The O 1s spectra of both samples displayed a single component at about 534 eV attributed to Si–O–H bonds. The absence of a peak corresponding to Si–O–Zn further supports the FTIR results, suggesting that no chemisorption of Zn occurred on the surface of KCC-1. Since the XANES analysis indicates the presence of Zn-silicates (discussed below), the absence of an O–Zn signal in XPS is likely due to the low proportion of O–Zn relative to O-Si even at the highest Zn content. Additionally, the lower sensitivity of XPS to the bulk further reduces the contribution of O-Zn signals from physisorbed Zn present within the bulk of the material.

3.7. X-Ray Absorption Spectroscopy

To determine the coordination state of Zn in the bulk of the doped KCC-1 samples, Zn K-edge XANES were analyzed. The normalized spectra of the 3-ZnKCC-1 and 6-ZnKCC-1 samples, along with the reference compound XANES profiles and the best linear combination fits are presented in Figure 7.

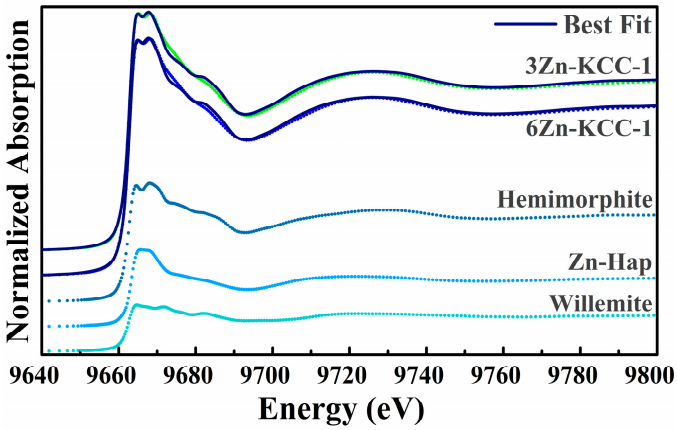

Figure 7. Zn K-edge normalized XANES spectra of 3-ZnKCC-1 (green dots) and 6-ZnKCC-1 (blue dots) along with the LCF (black full lines) shifted for clarity. The weighted contribution used for LCF is shown, and is vertically shifted for clarity.

An extensive dataset of Zn-K edge reference compounds from Ref. [35] was used to identify an optimal set of reference spectra (χ_i^{ref}). For both samples, the best fit indicated Hemimorphite ($Zn_4(Si_2O_7)(OH)_2.H_2O$) as the primary contributor, accounting for approximately 50% of the signal (Table 3), alongside 20% Willemite (Zn_2SiO_4). Additionally, a statistically significant contribution of about 30% from a Zn-hydroxyapatite-like (Zn-Hap) phase was identified to improve the LCF. Notably, contributions from Zn acetate, indicative of precursor residues, and ZnO, suggestive of segregated zinc oxide phases, were ruled out. Attempts to include an adsorbed Zn phase using the data from Ref. [35] were also unsuccessful.

Table 3. Weight percentages of reference compounds obtained from the LCF fitting of 3-ZnKCC-1 and 6-ZnKCC-1.

Standard	3-ZnKCC-1	6-ZnKCC-1
Hemimorphite	0.51 ± 0.05	0.54 ± 0.04
Zn-Hap	0.28 ± 0.02	0.28 ± 0.02
Willemite	0.21 ± 0.04	0.19 ± 0.03

The presence of Zn silicates in the samples confirms the incorporation of Zn into the KCC-1 structure. The inclusion of Zn modifies the connectivity within the amorphous silica network. Specifically, the structures of Hemimorphite and Willemite comprise ZnO_4 tetrahedra with distinct connectivities. In Hemimorphite, edge-sharing ZnO_4 tetrahedral pairs are linked to SiO_4 and OH units, while Willemite features a network of corner-sharing ZnO_4 and SiO_4 tetrahedra.

The identification of a Zn-Hap-like phase may initially appear unexpected, given the absence of Ca or P in the samples. However, it is important to recognize that XAFS is a local structural probe, sensitive to the oxidation state and to the short-range environment around the absorber, typically limited to the first few coordination shells. Consequently, LCF results should be interpreted as local structural analogies to reference compounds rather than definitive evidence of extended phases. Therefore, the Zn-Hap contribution likely reflects the presence of a Zn phase locally resembling Zn in hydroxyapatite, characterized by a more distorted Zn environment compared to Willemite or Hemimorphite. This environment consists of Zn ions in a 4–5-fold coordination with PO_4 groups and OH molecules. Given that P and Si contributions are indistinguishable in XAFS owing to their similar photoelectron scattering functions, this feature is most plausibly attributed to a highly disordered Zn-silicate phase.

Zinc silicates are highly promising materials with a significant potential for several industrial applications [42,43]. The results of our study confirm the complex nature of Zn incorporation in KCC-1 and opens up new avenues for further exploration of the Zn-KCC-1 potential in diverse fields such as photocatalysis [44], organic dyes removal [45], optoelectronics [46], and thermoregulating coatings [47].

4. Conclusions

In this study, pure KCC-1 and Zn-doped KCC-1 were successfully synthesized via a one-pot microemulsion technique followed by a hydrothermal treatment. A comprehensive characterization of the synthesized materials provided valuable insights into the doping process, structural evolution, and zinc incorporation limits within the silica matrix. The findings revealed a Zn saturation limit of approximately 6% which is attributed to competitive interactions between Zn species and silica precursors.

At lower Zn doping levels, the silica framework retained its structural integrity and characteristic fibrous morphology. However, with increasing Zn concentration, structural distortion became apparent, marked by a notable reduction in fiber density. At the highest loading of Zn, the fibrous structure was compromitted, and the particles exhibited a broad and not homogeneous size distribution. Furthermore, the study confirmed that Zn was incorporated into the silica matrix as silicate-type species, with no evidence of ZnO phase separation or surface chemical bonding.

These findings highlight the potential of Zn-doped KCC-1 for diverse applications including photocatalysis, environmental remediation, and sensing. Future research should focus on optimizing synthesis parameters, such as reaction conditions and precursor concentrations, to further enhance the structural and functional properties of Zn-doped KCC-1, paving the way for its broader application in advanced technologies.

Author Contributions: H.J.: Writing—review and editing, methodology, investigation, formal analysis, data curation; M.L.N.: writing—original draft, methodology, investigation, data curation; E.M.: methodology, investigation, formal analysis, data curation; F.B.: methodology, investigation, formal analysis, data curation; G.I.: methodology, investigation, formal analysis, data curation; I.C. methodology, investigation, formal analysis, data curation.; C.B.: validation, formal analysis, investigation, review and editing; C.M.: validation, formal analysis, investigation, review and editing, funding acquisition; L.T.: writing—review and editing, writing—original draft, supervision, resources, project administration, funding acquisition, conceptualization. All authors have read and agreed to the published version of the manuscript.

Funding: This research was funded by NextGenerationEU—PNRR Rome Technopole Innovation Ecosystem—CUP F83B22000040006; L.T. and E.M. acknowledge financial support through the Project PE 0000020 CHANGES—CUP [B83C22005060006], NRP Mission 4 Component 2 Investment 1.3, Funded by the European Union—NextGenerationEU". The authors from Roma Tre University gratefully acknowledge the Grant of Excellence Departments 2023–2027, MIUR (ARTICOLO 1, COMMI 314–337 LEGGE 232/2016).

Data Availability Statement: Data will be made available upon reasonable request.

Acknowledgments: We gratefully acknowledge Sergio Lo Mastro for the technical support in XRD and SEM analysis at the Interdepartmental facility LIME Roma Tre University. We acknowledge Elettra Sincrotrone Trieste for providing access to its synchrotron radiation facilities.

Conflicts of Interest: The authors declare no conflicts of interest. The funders had no role in the design of the study; in the collection, analyses, or interpretation of data; in the writing of the manuscript; or in the decision to publish the results.

References

1. Stöber, W.; Fink, A.; Bohn, E. Controlled Growth of Monodisperse Silica Spheres in the Micron Size Range. *J. Colloid Interface Sci.* **1968**, *26*, 62–69. [CrossRef]
2. Beck, J.S.; Vartuli, J.C.; Roth, W.J.; Leonowicz, M.E.; Kresge, C.T.; Schmitt, K.D.; Chu, C.T.W.; Olson, D.H.; Sheppard, E.W.; McCullen, S.B.; et al. A New Family of Mesoporous Molecular Sieves Prepared with Liquid Crystal Templates. *J. Am. Chem. Soc.* **1992**, *114*, 10834–10843. [CrossRef]
3. Zhao, D.; Feng, J.; Huo, Q.; Melosh, N.; Fredrickson, G.H.; Chmelka, B.F.; Stucky, G.D. Triblock Copolymer Syntheses of Mesoporous Silica with Periodic 50 to 300 Angstrom Pores. *Science* **1998**, *279*, 548–552. [CrossRef]
4. Melde, B.J.; Holland, B.T.; Blanford, C.F.; Stein, A. Mesoporous Sieves with Unified Hybrid Inorganic/Organic Frameworks. *Chem. Mater.* **1999**, *11*, 3302–3308. [CrossRef]
5. Polshettiwar, V.; Cha, D.; Zhang, X.; Basset, J.M. High-Surface-Area Silica Nanospheres (KCC-1) with a Fibrous Morphology. *Angew. Chemie Int. Ed.* **2010**, *49*, 9652–9656. [CrossRef]
6. Maity, A.; Polshettiwar, V. Dendritic Fibrous Nanosilica for Catalysis, Energy Harvesting, Carbon Dioxide Mitigation, Drug Delivery, and Sensing. *ChemSusChem* **2017**, *10*, 3866–3913. [CrossRef]
7. Maity, A.; Polshettiwar, V. Scalable and Sustainable Synthesis of Size-Controlled Monodisperse Dendritic Fibrous Nanosilica Quantified by e-Factor. *ACS Appl. Nano Mater.* **2018**, *1*, 3636–3643. [CrossRef]
8. Polshettiwar, V. Dendritic Fibrous Nanosilica: Discovery, Synthesis, Formation Mechanism, Catalysis, and CO_2 Capture–Conversion. *Acc. Chem. Res.* **2022**, *55*, 1395–1410. [CrossRef] [PubMed]
9. Hassan, N.S.; Jalil, A.A.; Twu, L.Y.; Fatah, N.A.A.; Hambali, H.U.; Hussain, I.; Firmansyah, M.L. Hydroisomerization of N-Hexane over Metal Oxides-Loaded Fibrous Silica Catalyst for Cleaner Fuel Production. *Int. J. Hydrogen Energy* **2023**, *48*, 20525–20537. [CrossRef]
10. Xu, L.; Wen, X.; Xu, C.; Bian, Y.; Chen, M.; Cheng, G.; Wu, C.E.; Qiu, J.; Chen, B.; Hu, X. Rare Earths Modified Highly Dispersed Fibrous Ni/KCC-1 Nanosphere Catalysts with Superb Low-Temperature CO_2 Methanation Performances. *Appl. Surf. Sci.* **2023**, *608*, 155258. [CrossRef]
11. Luo, Y.; Li, Y.; Wang, C.; Wang, J.; Liu, W.; Peng, H.; Wu, D. Highly Active CuO/KCC−1 Catalysts for Low-Temperature CO Oxidation. *Processes* **2022**, *10*, 145. [CrossRef]
12. Hitam, C.N.C.; Jalil, A.A.; Izan, S.M.; Azami, M.S.; Hassim, M.H.; Chanlek, N. The Unforeseen Relationship of Fe_2O_3 and ZnO on Fibrous Silica KCC-1 Catalyst for Fabricated Z-Scheme Extractive-Photooxidative Desulphurization. *Powder Technol.* **2020**, *375*, 397–408. [CrossRef]

13. Li, G.; Feng, W.; Luo, Y.; Yan, J.; Cai, Y.; Wang, Y.; Zhang, S.; Liu, W.; Peng, H. Unraveling FeOx Nanoparticles Confined on Fibrous Mesoporous Silica Catalyst Construction and CO Catalytic Oxidation Performance. *Catalysts* **2024**, *14*, 63. [CrossRef]
14. Ouyang, M.; Wang, Y.; Zhang, J.; Zhao, Y.; Wang, S.; Ma, X. Three Dimensional Ag/KCC-1 Catalyst with a Hierarchical Fibrous Framework for the Hydrogenation of Dimethyl Oxalate. *RSC Adv.* **2016**, *6*, 12788–12791. [CrossRef]
15. Gautam, P.; Dhiman, M.; Polshettiwar, V.; Bhanage, B.M. KCC-1 Supported Palladium Nanoparticles as an Efficient and Sustainable Nanocatalyst for Carbonylative Suzuki-Miyaura Cross-Coupling. *Green Chem.* **2016**, *18*, 5890–5899. [CrossRef]
16. Bai, Z.; Wang, J.; Yang, Q. Iron Doped Fibrous-Structured Silica Nanospheres as Efficient Catalyst for Catalytic Ozonation of Sulfamethazine. *Environ. Sci. Pollut. Res.* **2018**, *25*, 10090–10101. [CrossRef]
17. Palanichamy, K.; Umasankar, S.; Ganesh, S.; Sasirekha, N. Highly Coke Resistant Ni–Co/KCC-1 Catalysts for Dry Reforming of Methane. *Int. J. Hydrogen Energy* **2023**, *48*, 11727–11745. [CrossRef]
18. Pal, N.; Paul, M.; Bhaumik, A. Highly Ordered Zn-Doped Mesoporous Silica: An Efficient Catalyst for Transesterification Reaction. *J. Solid State Chem.* **2011**, *184*, 1805–1812. [CrossRef]
19. Shimada, S.; Otani, H.; Miura, A.; Sekiguchi, T.; Yokoyama, M. Synthesis and Characterization of Zn-Doped GaN Crystals by Simultaneous Carbothermal Reduction and Nitridation of Ga_2O_3 and ZnO. *J. Cryst. Growth* **2010**, *312*, 452–456. [CrossRef]
20. Fabbrizzi, L. The Design of Luminescent Sensors for Anions and Ionisable Analytes. *Coord. Chem. Rev.* **2000**, *205*, 85–108. [CrossRef]
21. Courthéoux, L.; Lao, J.; Nedelec, J.-M.; Jallot, E. Controlled Bioactivity in Zn-Doped Sol-Gel Derived SiO_2-CaO Bioactive Glasses. *J. Phys. Chem. C* **2008**, *112*, 13663–13667. [CrossRef]
22. Silvestre-Albero, J.; Serrano-Ruiz, J.C.; Sepúlveda-Escribano, A.; Rodríguez-Reinoso, F. Zn-Modified MCM-41 as Support for Pt Catalysts. *Appl. Catal. A Gen.* **2008**, *351*, 16–23. [CrossRef]
23. Chandra, D.; Mridha, S.; Basak, D.; Bhaumik, A. Template Directed Synthesis of Mesoporous ZnO Having High Porosity and Enhanced Optoelectronic Properties. *Chem. Commun.* **2009**, *17*, 2384–2386. [CrossRef] [PubMed]
24. Soci, C.; Zhang, A.; Xiang, B.; Dayeh, S.A.; Aplin, D.P.R.; Park, J.; Bao, X.Y.; Lo, Y.H.; Wang, D. ZnO Nanowire UV Photodetectors with High Internal Gain. *Nano Lett.* **2007**, *7*, 1003–1009. [CrossRef] [PubMed]
25. Shahul Hamid, M.Y.; Triwahyono, S.; Jalil, A.A.; Che Jusoh, N.W.; Izan, S.M.; Tuan Abdullah, T.A. Tailoring the Properties of Metal Oxide Loaded/KCC-1 toward a Different Mechanism of CO_2 Methanation by in Situ IR and ESR. *Inorg. Chem.* **2018**, *57*, 5859–5869. [CrossRef] [PubMed]
26. Hanif, M.A.; Ibrahim, N.; Md Isa, K.; Muhammad Ridwan, F.; Tuan Abdullah, T.A.; Jalil, A.A. Tailoring the Properties of Calcium Modified Fibrous Mesoporous Silica KCC-1 for Optimized Sulfur Dioxide Removal. *Microporous Mesoporous Mater.* **2022**, *330*, 111610. [CrossRef]
27. Farooqi, A.S.; Adnan, S.N.F.B.; Setiabudi, H.D.; Muhammad, S.A.F.S.; Ismail, S.; Aslam, S.; Abdullah, B. Syngas Production via Bi-Reforming of Methane Over Fibrous KCC-1 Stabilized Ni Catalyst. *Top. Catal.* **2023**, *66*, 235–246. [CrossRef]
28. Abdulkadir, B.A.; Rozi, M.N.M.; Norfairuzazuan, N.H.; Daud, N.A.M.; Setiabudi, H.D. Improved Photodegradation of Methylene Blue Using Cost-Effective and Renewable Fe-Supported Fibrous Nano-Silica from Palm Oil Fuel Ash. *Top. Catal.* **2024**. [CrossRef]
29. Marconi, E.; Luisetto, I.; Di Carlo, G.; Staccioli, M.; Tuti, S.; Tortora, L. 3-APTES on Dendritic Fibrous Mesoporous Silica Nanoparticles for the PH-Controlled Release of Corrosion Inhibitors. *Nanomaterials* **2023**, *13*, 2543. [CrossRef]
30. Bunker, G. *Introduction to XAFS: A Practical Guide to X-Ray Absorption Fine Structure Spectroscopy*; Cambridge University Press: New York, NY, USA, 2010; ISBN 9780521767750.
31. Jark, W.; Eichert, D.; Luehl, L.; Gambitta, A. Optimisation of a Compact Optical System for the Beamtransport at the X-Ray Fluorescence Beamline at Elettra for Experiments with Small Spots. *Adv. X-Ray/EUV Opt. Components IX* **2014**, *9207*, 92070G. [CrossRef]
32. Karydas, A.G.; Czyzycki, M.; Leani, J.J.; Migliori, A.; Osan, J.; Bogovac, M.; Wrobel, P.; Vakula, N.; Padilla-Alvarez, R.; Menk, R.H.; et al. An IAEA Multi-Technique X-Ray Spectrometry Endstation at Elettra Sincrotrone Trieste: Benchmarking Results and Interdisciplinary Applications. *J. Synchrotron Radiat.* **2018**, *25*, 189–203. [CrossRef] [PubMed]
33. Meneghini, C.; Mobilio, S.; Bardelli, F.; Prestipino, C. ESTRA and FitEXA. In *International Tables for Crystallography*; International Union of Crystallography: Chester, UK, 2024; Volume I.
34. Benfatto, M.; Meneghini, C. A Close Look into the Low Energy Region of the XAS Spectra: The XANES Region. In *Synchrotron Radiation*; Mobilio, S., Boscherini, F., Meneghini, C., Eds.; Springer: Berlin/Heidelberg, Germany, 2015; pp. 213–240.
35. De Giudici, G.; Meneghini, C.; Medas, D.; Buosi, C.; Zuddas, P.; Iadecola, A.; Mathon, O.; Cherchi, A.; Kuncser, A.C. Coordination Environment of Zn in Foraminifera *Elphidium aculeatum* and *Quinqueloculina seminula* Shells from a Polluted Site. *Chem. Geol.* **2018**, *477*, 100–111. [CrossRef]
36. Ravel, B.; Newville, M. ATHENA, ARTEMIS, HEPHAESTUS: Data Analysis for X-Ray Absorption Spectroscopy Using IFEFFIT. *J. Synchrotron Radiat.* **2005**, *12*, 537–541. [CrossRef] [PubMed]
37. Drake, B.L. Appendix A: Element Guide. In *Advances in Portable X-Ray Fluorescence Spectrometry*; The Royal Society of Chemistry: London, UK, 2022.

38. Hitam, C.N.C.; Jalil, A.A.; Raji, Y.O. Fabrication of Fibrous Silica Zinc (FSZn) Composite for Enhanced Photocatalytic Desulphurization. *Top. Catal.* **2020**, *63*, 1169–1181. [CrossRef]
39. Ali, A.M.; Harraz, F.A.; Ismail, A.A.; Al-Sayari, S.A.; Algarni, H.; Al-Sehemi, A.G. Synthesis of Amorphous ZnO-SiO_2 Nanocomposite with Enhanced Chemical Sensing Properties. *Thin Solid Films* **2016**, *605*, 277–282. [CrossRef]
40. Abdulrasheed, A.A.; Jalil, A.A.; Hamid, M.Y.S.; Siang, T.J.; Fatah, N.A.A.; Izan, S.M.; Hassan, N.S. Dry Reforming of Methane to Hydrogen-Rich Syngas over Robust Fibrous KCC-1 Stabilized Nickel Catalyst with High Activity and Coke Resistance. *Int. J. Hydrogen Energy* **2020**, *45*, 18549–18561. [CrossRef]
41. Mosaad Awad, M.; Hussain, I.; Ganiyu, S.A.; Alhooshani, K. Highly Active Nickel-Based Fibrous Silica ZnO (NSZF) Catalyst for Efficient Syngas Production through Dry Reforming of Methane. *Fuel* **2025**, *380*, 133261. [CrossRef]
42. Bouatrous, M.; Bouzerara, F.; Bizot, Q. Sonochemistry Synthesis of Zinc Silicate Ceramic Nanoparticles and Their Characterization. *J. Inorg. Organomet. Polym. Mater.* **2024**, *34*, 1931–1943. [CrossRef]
43. Beglaryan, H.; Isahakyan, A.; Zulumyan, N.; Melikyan, S.; Terzyan, A. A Study of Zinc Silicate Phases Produced via a Simplified Method. *J. Therm. Anal. Calorim.* **2023**, *148*, 3249–3262. [CrossRef]
44. Li, Y.; Tan, Y.; Zhou, Z.; Yan, T.; Yu, L.; Zeng, J. Photocatalytic Activity of Zinc Oxide/Hemimorphite/Silica Aerogel Materials: Performance and Mechanism. *J. Mater. Sci. Mater. Electron.* **2024**, *35*, 1725. [CrossRef]
45. Qin, X.; Cai, H.; Wang, F.; Xu, Y. Hydrothermal Synthesis of Zinc Silicate Nanomaterials for Organic Dyes Removal from Aqueous Solutions. *Silicon* **2024**, *16*, 6031–6039. [CrossRef]
46. Afandi, M.M.; Park, H.; Lee, S.; Kim, J. Yellow Electroluminescence from Metastable Zinc Silicate in an Electrolyte-Assisted Silicon Semiconductor Structure. *J. Lumin.* **2024**, *275*, 120794. [CrossRef]
47. Baghramyan, V.V.; Sargsyan, A.A.; Knyzyan, N.B.; Harutyunyan, V.V.; Badalyan, A.H.; Grigoryan, N.E.; Aprahamian, A.; Manukyan, K.V. Pure and Cerium-Doped Zinc Orthosilicate as a Pigment for Thermoregulating Coatings. *Ceram. Int.* **2020**, *46*, 4992–4997. [CrossRef]